Sensors and Materials, Vol. 38, No. 3 (2026) 1119–1133
MYU Tokyo

S & M 4367

Density Functional Theory and Experimental Study of Detection of Dissolved Gas in Transformer Oil on Ru-doped 2D MoO_{3-x} Monolayer

Baiquan Chen,[1] Zilan He,[1] Yueping Liu,[1]
Bangfa Chen,[1] Shaohui Liu,[1] and Sicheng Zhao[2*]

[1]Foshan Power Supply Bureau of Guangdong Power Grid Co., Ltd.,
No. 16, Maogang East Road, Foshan 528000, China
[2]China Southern Power Grid Research Institute, No. 11, Kexiang Road, Guangzhou 510700, China

(Received September 8, 2025; accepted January 6, 2026)

Keywords: dissolved gas analysis, transformer oil, molybdenum trioxide, density functional theory, doping

Dissolved gas analysis (DGA) has emerged as a noninvasive diagnostic method for assessing transformer health, enabling the timely detection of incipient faults through the quantitative monitoring of evolving gas concentrations in dielectric fluids. On the basis of first-principles calculations integrated with experimental investigations, in this study, we systematically examine the adsorption characteristics and gas sensing mechanisms of different molybdenum oxide structures, particularly with respect to ruthenium doping, in response to dissolved gases such as carbon monoxide (CO), acetylene (C_2H_2), and hydrogen (H_2) present in oil-immersed transformers. The sensitivities of molybdenum trioxide (MoO_3), MoO_{3-x}, Ru-doped MoO_3 (MoO_3@Ru), and Ru-doped high-defect-concentration MoO_{3-x} (H-MoO_{3-x}@Ru) to these gases were evaluated through adsorption energy, charge distribution, and band structure changes. Results showed that oxygen vacancies in molybdenum oxide enhance CO absorption and significantly affect electrical conductivity. Although H-MoO_{3-x} has a high carrier concentration, C_2H_2 adsorption has a minimal impact on its electronic properties, limiting its sensor application potential. Ru atoms are most stable at terminal or oxygen-deficient sites in MoO_3 and MoO_{3-x}. The H-MoO_{3-x}@Ru structure exhibits strong CO adsorption performance, making it a promising candidate for CO gas sensing. Overall, Ru-modified molybdenum oxide materials show great potential for detecting dissolved gases in transformer oil.

1. Introduction

In the complex framework of power system operations, particularly within transmission, transformation, and distribution networks, electric power transformers play a crucial role in ultrahigh-voltage grids.(1,2) The operational integrity and optimal performance of these transformers are essential for maintaining the stability and continuous functioning of the entire

---

*Corresponding author: e-mail: zhaosc9210@163.com
https://doi.org/10.18494/SAM5928

ISSN 0914-4935
https://myukk.org/

power infrastructure.(3) Continuous monitoring of internal anomalies in power transformers, along with thorough evaluation of potential defects, is vital for preventing sudden insulation failures or malfunctions caused by aging.(4) This preventive strategy ensures the reliability of power transformers and supports a consistent electricity supply. Currently, oil-immersed transformers are the most prevalent type and serve as key components in modern power systems. However, long-term operation inevitably leads to insulation degradation, which may result in overheating or partial discharge phenomena. These issues can potentially trigger large-scale power outages.(5) Such faults initiate a series of chemical reactions within the transformer oil, releasing gases such as H_2, CH_4, CO, CO_2, and C_2H_2.(4,6) Therefore, analyzing the dissolved gases in transformer oil provides a practical and effective method for assessing transformer health.(7) Semiconductor gas sensors, known for their compact design, high sensitivity, cost-effectiveness, fast response and recovery times, and low power consumption, have gained extensive application in various environmental sensing fields.(8,9)

Numerous researchers have devoted significant efforts to advancing the detection of fault characteristic gases in transformer oil, encompassing both theoretical simulations and experimental validation.(10–12) Ideal gas sensor materials should possess a porous structure and a large specific surface area.(13) Commonly employed materials include transition metal oxides (TMOs), transition metal sulfides, organic-based chemical resistive gas sensor materials, and carbon-based materials.(14–17) In recent years, TMOs have attracted significant attention because of their excellent chemical reactivity toward various gases. This category includes SnO_2, ZnO, TiO_2, WO_3, and MoO_3.(18–20) Gui *et al.* conducted density functional theory (DFT) calculations to evaluate the sensitivity of Co-doped TiO_2.(21) Their results indicate that Co-doped TiO_2 exhibits superior adsorption capabilities, making it a promising candidate for detecting H_2, C_2H_2, and C_2H_4. Liu *et al.* developed an ultrasensitive gas sensor for low-concentration SO_2 detection using single-atom Ni anchored on oxygen-vacancy-rich SnO_2 nanorods as the sensing material.(22) The sensor demonstrates a response value of 48 to 20 ppm SO_2, with a detection limit of 100 ppb. The synergistic effects between Ni single atoms and adjacent oxygen vacancies on the SnO_2 surface enhance SO_2 adsorption and chemisorbed oxygen activation. Liu *et al.* investigated the adsorption behavior of dissolved gases in typical transformer oil using Pd-atom-cluster-modified SnO_2 nanowires.(23) DFT calculations combined with experimental data show that Pd-4 significantly enhances the sensitivity of SnO_2 to H_2 and C_2H_2. These findings suggest that metal atom doping can alter the electronic structure of the system, thereby affecting the adsorption and desorption behaviors of target molecules and ultimately improving the sensor's sensitivity and response performance.(6,24)

Molybdenum trioxide (MoO_3), a quintessential TMO, showcases distinctive physicochemical traits attributed to its α-MoO_3 orthorhombic phase, characterized by a two-dimensional layered architecture.(25) In contemporary research landscapes, this material has attracted significant attention across disciplines including biology, catalysis, sensing technology, and electronic devices.(26) The electronic configuration and surface characteristics of α-MoO_3 are amenable to manipulation not solely through the incorporation of defects but also via heteroatom doping strategies, which in turn affect the electron spin polarization and redistribution of electron states.(27) A case in point is the work of Li *et al.*, who engineered an exceptionally sensitive NO_2

gas sensor utilizing MoO_3, celebrated for its superior selectivity and reversibility.(28) MoO_3 nanobelts, synthesized employing vapor transport methodologies, manifest remarkable sensitivity at an optimal operational temperature of 125 °C, achieving a detection threshold as minimal as 24 ppb, alongside commendable selectivity and reversibility. Furthermore, scholarly endeavors have revealed that the introduction of metallic dopants such as iron, cobalt, nickel, and tungsten into the MoO_3 lattice can amplify its responsiveness to specific gases.(29,30) Nonetheless, comprehensive theoretical explorations concerning noble-metal-doped MoO_3 variants with diverse defect profiles for gas sensing applications in transformer oils remain scarce in the scientific literature.

In this study, we leverage the computational prowess of CP2K software to devise adsorption models for ruthenium-doped pristine MoO_3 and defective MoO_{3-x} systems, targeting the detection of fault gases in transformers. Through meticulous examination of the most stable adsorption geometries, adsorption energies (E_{ad}), charge transfer dynamics, densities of states (DOS), and band gaps (E_g), we delve into the adsorption tendencies of molybdenum oxide derivatives towards CO, C_2H_2, and H_2. Oxygen vacancies in molybdenum oxide enhance CO adsorption and significantly affect electrical conductivity. Although high-defect-concentration MoO_{3-x} (H-MoO_{3-x}) exhibits a high carrier concentration, the adsorption of C_2H_2 has a minimal effect on its electronic properties, thereby limiting its potential for sensor applications. Ru atoms are most stable when located at terminal or oxygen-deficient sites in both MoO_3 and MoO_{3-x}. The Ru-doped MoO_{3-x} (H-MoO_{3-x}@Ru) structure has been experimentally demonstrated to exhibit a strong CO adsorption capability. Our findings provide invaluable theoretical insights and practical guidance for the synthesis of advanced molybdenum-based sensing materials and the development of gas sensors .tailored for monitoring characteristic fault gases in transformer oil environments.

2. Materials and Methods

2.1 Computational details

The theoretical simulation based on DFT is performed using the Quickstep module within the CP2K software package. Specifically, the Kohn–Sham equation is solved by the Gaussian plane wave (GPW) method, which combines a double-zeta polarized Gaussian basis set optimized for condensed systems with a plane wave basis set (with an energy cutoff of 400 Ry). Additionally, the Goedecker–Teter–Hutter (GTH) pseudopotential in the ultrasoft mode is employed to describe ion–electron interactions. The Brillouin zone sampling density at the K-point for each model is ensured to be no less than 0.05 $Å^{-1}$. Structural optimization is achieved through the Broyden–Fletcher–Goldfarb–Shanno (BFGS) minimization algorithm. In this process, convergence criteria are set as follows: geometric changes converge within 3×10^{-3} Bohr, the root mean square (RMS) of geometric changes converges within 1.5×10^{-3} Bohr, forces converge within 4.5×10^{-4} Hartree/Bohr, and the RMS of forces converges within 3×10^{-4} Hartree/Bohr. Given that the choice of the functional significantly affects both the efficiency and accuracy of DFT simulations, the GGA-PBE functional is utilized for structure optimization tasks, supplemented by the DFT-D3 dispersion correction scheme. Meanwhile, the B3LYP functional is adopted to achieve precise electronic structure calculations through the following procedure. Construct the minimal unit cell of MoO_3, develop a 5 × 5 × 1 supercell structure model of MoO_3, and subsequently introduce oxygen vacancies to obtain the defective MoO_{3-x} model. Vacuum layers for all surface models are set to 15 Å to prevent spurious interlayer interactions between adjacent units.

CO or C_2H_2 was introduced into the stable model to construct the corresponding adsorption model. Geometric optimization and parameter calculations of the system were performed using the Quickstep module in the CP2K software, enabling an investigation into the electronic structure characteristics of monolayer CO/C_2H_2–MoO_3 and CO/C_2H_2–MoO_{3-x} with adsorbed gases. Finally, the adsorption models for the optimized CO and C_2H_2 gas molecules on the defective MoO_{3-x} crystal plane were established. The most stable adsorption configuration and the corresponding adsorption performance parameters were subsequently calculated. E_{ad} can be calculated using the following equation:

$$E_{ad} = E_{\mathrm{MoO3}-x/\mathrm{gas}} - E_{\mathrm{MoO3}-x} - E_{gas}. \tag{1}$$

Here, $E_{\mathrm{MoO3}-x/\mathrm{gas}}$, $E_{\mathrm{MoO3}-x}$, and E_{gas} represent the energy of the gas adsorption system, that of the single-layer MoO_{3-x}, and that of a single gas molecule, respectively. If $E_{ad} < 0$, it indicates that the adsorption process is exothermic and can proceed spontaneously. Furthermore, the larger the absolute value of E_{ad}, the greater the total energy change in the model and the stronger the interaction between the gas molecules and the surface. In this study, the Hirshfeld method was employed to analyze and quantify the charge transfer (Q_t) between the gas molecule and the MoO_{3-x} surface. The charge transfer is calculated as

$$Q_t = Q_a - Q_b, \tag{2}$$

where Q_a represents the total charge of the gas molecule after adsorption and Q_b denotes the free charge of the gas molecule prior to adsorption.

On the basis of the first-principles calculations within the framework of DFT, nondefective MoO_3 and defective MoO_{3-x} models were constructed, and the doping mechanism was investigated to elucidate how Ru doping affects the structural and electronic properties of MoO_3 with various degrees of defects. The adsorption energy of Ru doping, denoted as E_{form}, can be calculated using

$$E_{form} = E_{total} - E_{MO} - E_{dopant}. \tag{3}$$

Herein, E_{total} represents the total energy of the system after doping, E_{MO} corresponds to the energy of the molybdenum oxide matrix, and E_{dopant} signifies the energy of the doped metal component.

Then, CO and H_2 molecules were introduced into the stabilized doping model to construct corresponding adsorption configurations. The geometric optimization and parameter calculations of the system were performed using the Quickstep module in the CP2K software package, enabling a detailed exploration of the electronic structure characteristics of monolayer MoO_3@Ru and MoO_{3-x}@Ru systems in the presence of adsorbed gases. The adsorption models of the optimized gas molecules on the crystal planes of MoO_3@Ru and MoO_{3-x}@Ru were constructed. Subsequently, the most stable adsorption structures and their corresponding adsorption performance parameters were calculated. The adsorption energy can be calculated using

$$E_{ad}' = E_{\mathrm{MoO3@Ru/gas}} - E_{\mathrm{MoO3@Ru}} - \mathrm{E}_{gas}' \tag{4}$$

where $E_{\mathrm{MoO3@Ru/gas}}$, $E_{\mathrm{MoO3@Ru}}$, and E_{gas}' represent the total energy of the gas adsorption system, the energy of a single MoO_3@Ru structure, and the energy of an isolated gas molecule (CO or H_2), respectively. Similarly, the Hirshfeld analysis method was employed to investigate and quantify the Q_t between the molecule and the MoO_3@Ru surface.

2.2 Synthesis of MoO_{3-x}@Ru

The experiment involved taking 100 mg of MoS_2 and annealing it in air at 350 °C for 90 min. The resulting product was then homogeneously dispersed in a 10 ml 45% ethanol/water mixture by sonication for 1 h. The dispersion was transferred to a supercritical carbon dioxide device, which consisted of a stainless-steel autoclave, a heating jacket, and a temperature controller. The autoclave was heated to 80 °C and filled with CO_2 at a pressure of 20 MPa. The reaction mixture was maintained at the designated pressure and temperature for three hours. Upon completion of the reaction, the autoclave was cooled to room temperature, and the supernatant was collected by centrifugation at 6000 r min^{-1} for 15 min to eliminate the large precipitate. Subsequently, the supernatant was dried in a constant-temperature oven at 60 °C. 10 mg of the pre-prepared H-MoO_{3-x} sample was dispersed in 10 mL of deionized water and sonicated in a water bath to achieve a uniform dispersion. Subsequently, 2 μL of a $RuCl_3$ solution (10 mg mL^{-1}, Ru basis) was added dropwise, and the mixture was stirred in the dark for 3 h. After the reaction, the mixture was dried in a vacuum oven at 60 °C, affording the final powder product H-MoO_{3-x}@Ru.

2.3 Material characterization

The crystal structure of the samples was characterized by X-ray diffraction (XRD) using a Rigaku SmartLab SE instrument, which enabled the determination of the crystal type, lattice parameters, and degree of crystallinity. Transmission electron microscopy (TEM, FEI Talos F200x G2) was employed to investigate the morphological features of the samples. The Ru content in the composite sample was determined via ICP-OES/MS (Agilent 5110).

2.4 Sensor fabrication and performance testing

The prepared samples were thoroughly mixed with anhydrous ethanol in an agate mortar to form a homogeneous paste, which was then uniformly coated onto a ceramic substrate (7 × 13.4 mm^2) containing Au-Pd interdigital electrodes to fabricate a consistent gas-sensing layer. The coated samples were annealed in ambient air at 200 ℃ for 2 h to improve thermal stability and measurement reproducibility. All gas-sensing measurements were conducted at 25 ℃ and 23% relative humidity within a sealed gas chamber equipped with a precision-controlled gas delivery system. Real-time electrical resistance was monitored continuously using a Keithley 6500 electrometer. By introducing carbon monoxide at varying concentrations into the test tube, the variation in the sensor's resistance intensity with respect to gas concentration was measured and recorded.

3. Results and Discussion

3.1 Structural analysis

3.1.1 Monolayer MoO_3 and MoO_{3-x} models

The structures of nondefective MoO_3, MoO_{3-x} with low defect concentration (L-MoO_{3-x}), and H-MoO_{3-x} were optimized, and the model structures are shown in Fig. 1. The results showed that the introduction of oxygen defects will destroy the lattice symmetry of MoO_3 and introduce

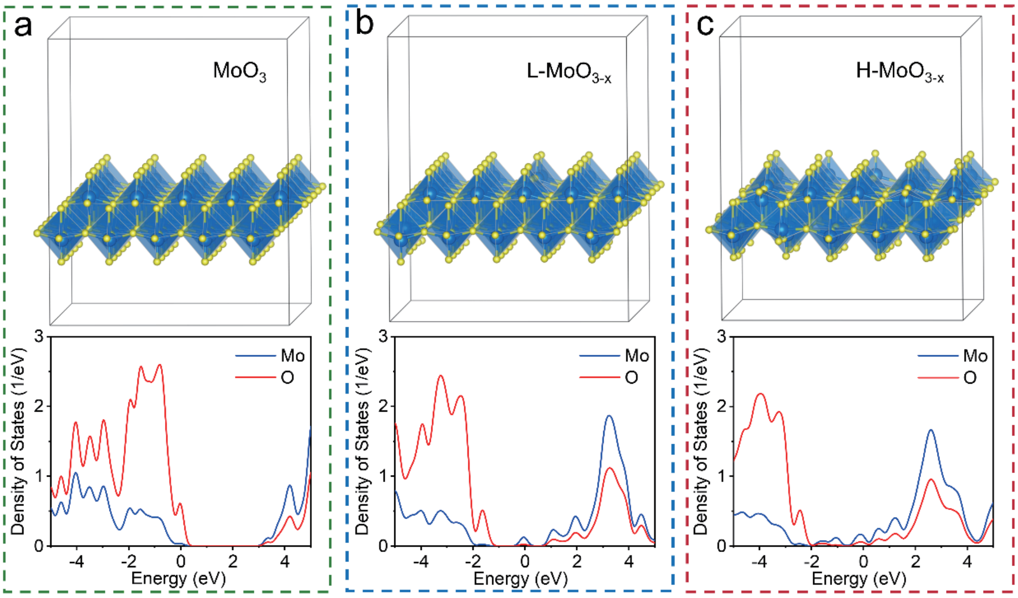

Fig. 1. (Color online) (a) Atomic structures of nondefective MoO_3 and the corresponding density of electronic states. (b) Atomic structures of L-MoO_{3-x} and the corresponding density of electronic states. (c) Atomic structures of H-MoO_{3-x} and the corresponding density of electronic states. The blue atom is Mo and the yellow atom is O.

a disordered atomic arrangement. The energy gap E_g of nondefective MoO_3 is 3.33 eV, and its valence band top is dominated by O electrons, whereas the conduction band bottom is dominated by Mo electrons. The oxygen defect causes the appearance of impurity energy levels dominated by Mo electrons in the band gap and the right shift of the Fermi level, which means that the oxygen defect will achieve the excessive enrichment of electrons around Mo atoms and significantly regulate the band gap. The energy gap of L-MoO_{3-x} containing about 1.3% oxygen defects is reduced to 0.97 eV. Moreover, the energy gap of H-MoO_{3-x} containing about 5.3% oxygen defects is reduced to 0.45 eV, meaning that the conductivity is improved and the resistance is reduced.

3.1.2 MoO_3@Ru and H-MoO_{3-x}@Ru monolayer models

Subsequently, the effect of the introduction of Ru on the MoO_3 and H-MoO_{3-x} monolayer structure was investigated. After the adsorption of Ru atoms, the structure diagram for MoO_3@Ru and MoO_{3-x}@Ru is as shown in Figs. 2(a) and 2(d). After structure optimization, it is found that the doping sites of Ru are all located at the end oxygen. Ru adsorbed on the surface of MoO_3 will form four kinds of Ru–O bonds with the lengths of 2.00, 1.99, 1.98, and 2.07 Å and the adsorption energy E_{ad} of –4.7 eV. Ru adsorbed on the surface of H-MoO_{3-x} will form two kinds of Ru–O bonds with the lengths of 1.91 and 1.96 Å and the adsorption energy of –4.56 eV, which means that the adsorption strength of Ru and the system containing defects is weaker than that of the nondefective system. The internal reason is that the oxygen defects mentioned above will lead to an electron-rich MoO_3 system. The binding of Ru to oxygen at the surface end is

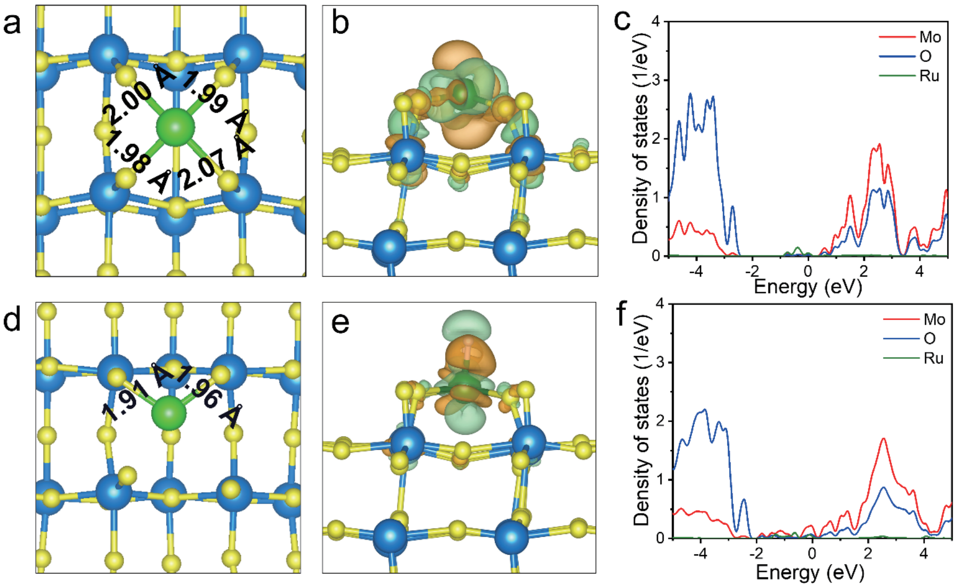

Fig. 2. (Color online) (a) Atomic structures, (b) Ru differential charge density, and (c) the corresponding DOS of MoO_3@Ru. (d) Atomic structures, (e) Ru differential charge density, and (f) the corresponding DOS of H-MoO_{3-x}@Ru. The blue atom is Mo, the yellow atom is O, the green atom is Ru, the orange represents the electron-enriched region, the green represents the electron-deficient region, and the isosurface is 0.003 e/$Å^2$.

inhibited. According to Hirshfeld's method, the amounts of charge transfer of Ru to MoO_3 and defective H-MoO_{3-x} are 0.472 e and 0.428 e [Figs. 2(b) and 2(e)], respectively. Ru loses fewer electrons on the surface of defective MoO_{3-x}, which confirms its weaker binding strength. The study of the electronic structure revealed that the density of state spectrum of Ru–MoO_3 changed significantly, and the energy gap decreased from 3.33 to 0.54 eV. By comparing the DOS maps of Mo, O, and Ru, the electronic density of state is found to originate mainly from Ru. The whole DOS curve shifts to the left owing to Ru atom activation. Similarly, although the energy band E_g of the adsorbed Ru atom of H-MoO_{3-x} also decreases, the change is not significant (0.45 to 0.38 eV) because of the weak electronic coupling between Ru and H-MoO_{3-x}.

3.2 Gas Sensitivity of MoO_3 and MoO_{3-x} monolayers

3.2.1 CO sensitivity

The bond length of the linear CO molecule is 1.150 Å. From Figs. 3(a) and 3(b), the adsorption energy of monolayer MoO_3 for CO is found to be –0.311 eV. Upon adsorption, the band gap

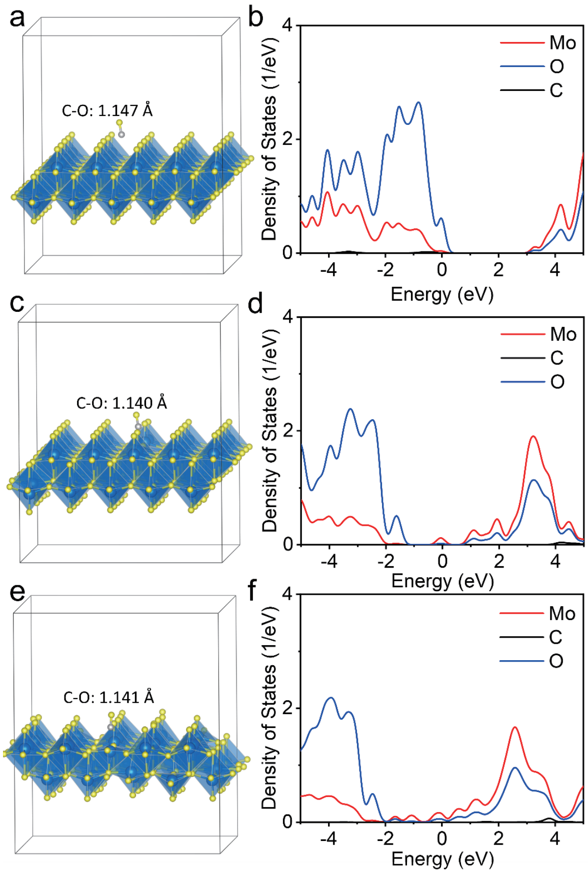

Fig. 3. (Color online) (a, b) CO adsorption model of MoO_3 and DOS diagram of the corresponding model. (c, d) CO adsorption model of L-MoO_{3-x} and DOS diagram of the corresponding model. (e, f) CO adsorption model of H-MoO_{3-x} and DOS diagram of the corresponding model. The blue atom is Mo, the yellow atom is O, and the gray atom is C.

decreases from 3.33 to 3.27 eV, and the bond length of CO is reduced to 1.147 Å. The results of the differential charge distribution analysis indicate that CO loses only 0.004 electrons. By comparing the subtle changes before and after adsorption, we can infer that defect-free MoO_3 crystals exhibit limited sensitivity in detecting CO. The same method was employed to investigate the gas-sensitive responses of L-MoO_{3-x} and H-MoO_{3-x} to CO, as well as their adsorption structure and electronic properties. Figures 3(c) and 3(d) show that the adsorption energy of CO molecules on the surface of L-MoO_{3-x} is −0.577 eV, with the bond length of CO decreasing to 1.140 Å. On the basis of the differential charge distribution analysis results, it can be inferred that CO loses 0.19 electrons. The adsorption of CO leads to a reduction in the E_g of L-MoO_{3-x} from 0.974 to 0.922 eV. Compared with L-MoO_{3-x}, as shown in Figs. 3(e) and 3(f), the adsorption energy of CO molecules on the surface of H-MoO_{3-x} is determined to be −1.188 eV, with the bond length of CO decreasing to 1.141 Å. The analysis of the differential charge distribution revealed that CO loses 0.20 electrons. Furthermore, the adsorption of CO results in a reduction of the E_g of H-MoO_{3-x} from 0.452 to 0.405 eV. It can be observed that the introduction of defects enhances the adsorption capacity of molybdenum oxide for CO molecules. Simultaneously, there is a significant alteration in electrical conductivity, which indicates an improvement in detection capability.

3.2.2 C_2H_2 sensitivity

The same method was further employed to analyze the gas-sensing responses of MoO_3, L-MoO_{3-x}, and H-MoO_{3-x} toward C_2H_2. The bond length of the carbon–carbon triple bond in the C_2H_2 molecule is 1.211 Å. The adsorption energy of monolayer MoO_3 for C_2H_2 is −0.32 eV [Figs. 4(a) and 4(b)]. After adsorption, the bandgap decreases from 3.33 to 1.68 eV, indicating an increase in the electrical conductivity of the entire system. Notably, the bond length of the carbon–carbon triple bond in CO remains largely unchanged after adsorption. The differential charge distribution analysis results showed that C_2H_2 gains 0.03 e. Therefore, it can be concluded that compared with CO, MoO_3 exhibits a more favorable detection performance for C_2H_2. From Figs. 4(b) and 4(c), the adsorption energy of C_2H_2 molecules on the surface of L-MoO_{3-x} was determined to be −0.73 eV, with the carbon–carbon bond length increasing to 1.217 Å. The analysis of the differential charge distribution revealed that C_2H_2 lost 0.14 electrons. The adsorption of C_2H_2 resulted in a reduction of the E_g of L-MoO_{3-x} from 0.97 to 0.93 eV. In Figs. 4(e) and 4(f), we can see that the adsorption energy of C_2H_2 molecules on the H-MoO_{3-x} surface is −1.02 eV, with the carbon–carbon bond length increasing to 1.218 Å. From the results of the analysis of the differential charge distribution, we can infer that C_2H_2 loses 0.13 electrons. Furthermore, the adsorption of C_2H_2 results in a reduction of the bandgap of H-MoO_{3-x} from 0.45 to 0.41 eV. For C_2H_2 molecules, defects in molybdenum oxide can enhance the adsorption capacity of gas molecules; however, this may lead to a reduction in detection sensitivity.

3.3 Sensitivity of MoO_3@Ru and H-MoO_{3-x}@Ru monolayers to H_2 and CO

The incorporation of precious metals generally enhances the gas-sensing sensitivity of materials. The same method was also used to analyze the gas-sensitive responses of MoO_3@Ru

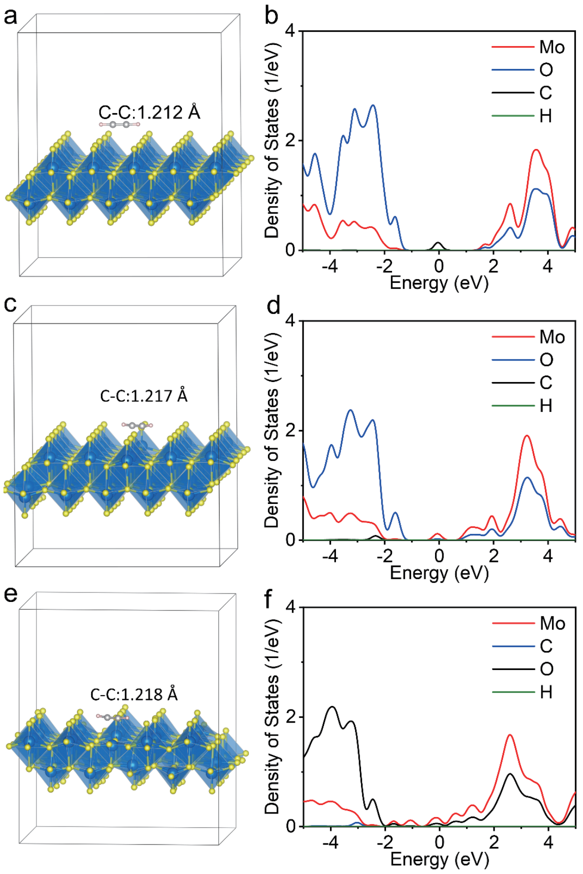

Fig. 4. (Color online) (a, b) C_2H_2 adsorption model of MoO_3 and DOS diagram of the corresponding model. (c, d) C_2H_2 adsorption model of L-MoO_{3-x} and DOS diagram of the corresponding model. (e, f) C_2H_2 adsorption model of H-MoO_{3-x} and DOS diagram of the corresponding model. The blue atom is Mo, the yellow atom is O, the gray atom is C, and the pink atom is H.

and H-MoO_{3-x}@Ru to H_2 and CO, and their adsorption structures and electronic properties were analyzed. According to Fig. 5(a), the H_2 gas molecule is a simple diatomic molecule with a bond length of 0.74 Å. After structural optimization, H_2 molecules became activated because of electron transfer. Consequently, the H–H bond length increased to 1.13 Å, whereas the Ru–H bond lengths were both measured to be 1.60 Å. The charge density near the H-bond exhibits a substantial increase, with the Ru atom serving as the central site of electron depletion [Fig. 5(b)]. This results in the transfer of 0.10 electrons from MoO_3@Ru to H_2, thereby enabling H_2 to possess an adsorption energy of −1.23 eV on the MoO_3@Ru surface. The DOS following H_2 adsorption is presented in Fig. 5(c). Electronic coupling led to an increase in the E_g of MoO_3@Ru from 0.54 to 0.62 eV, indicating a reduction in the electrical conductivity of the entire system post-adsorption. It can be observed from Fig. 4(e) that the H-H bond length of the H_2 molecules adsorbed on the surface of H-MoO_{3-x}@Ru increases to 0.82 Å, indicating that the activation level of H_2 is significantly lower than that of the H_2 molecules adsorbed on the surface of MoO_3@Ru. Energy studies revealed that the adsorption energy of H_2 under these conditions is −0.43 eV, which is considerably lower than the −1.23 eV observed for H_2 adsorbed on the surface

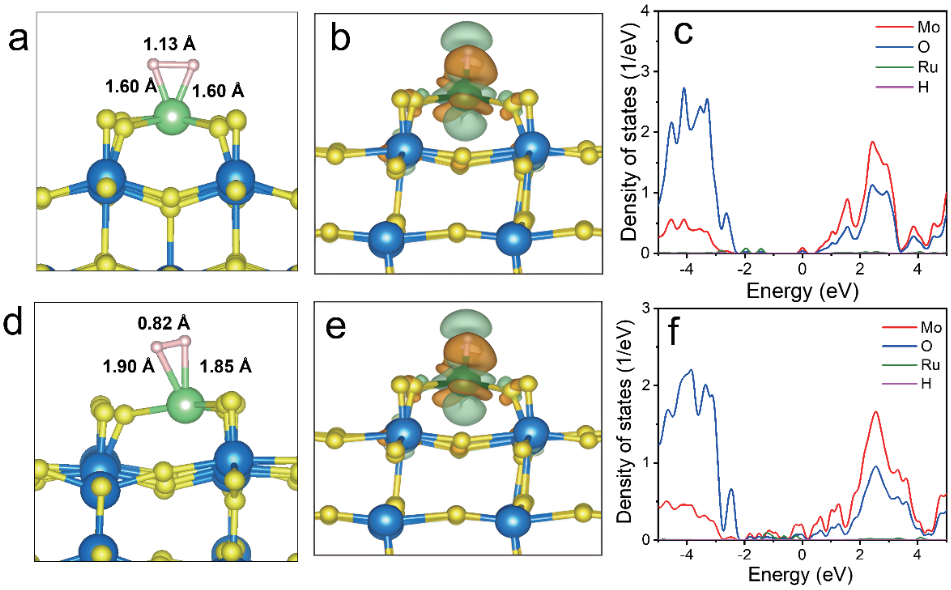

Fig. 5. (Color online) (a) H_2 adsorption model of MoO_3@Ru. (b) Differential charge density diagram of the corresponding model of H_2-MoO_3@Ru. The orange region represents an increase in electron density, whereas the green region denotes a decrease in electron density. (c) DOS diagram of the corresponding model of H_2-MoO_3@Ru. (d) H_2 adsorption model of H-MoO_{3-x}@Ru. (e) Differential charge density diagram of the corresponding model. (f) DOS diagram of the corresponding model of H-MoO_{3-x}@Ru. The blue atom is Mo, the yellow atom is O, and the gray atom is C.

of MoO_3@Ru. Additionally, the results of electron configuration analyses indicate that only 0.06 electrons are transferred from H-MoO_{3-x}@Ru to H_2. The adsorption of H_2 induces a minor reduction in the E_g of MoO_{3-x}@Ru from 0.381 to 0.379 eV, indicating that the adsorption of H_2 has a negligible impact on the electrical conductivity of MoO_{3-x}@Ru. The defect-induced electron enrichment substantially suppressed the electron coupling between H_2 and Ru, thereby weakening the adsorption strength of H_2 molecules. This suggests that, in comparison with MoO_3@Ru, H-MoO_{3-x}@Ru is not an optimal material for H_2 detection. For CO detection, CO adsorption models and DOS diagrams of MoO_3@Ru and H-MoO_{3-x}@Ru are shown in Fig. 6. Energy studies indicate that the adsorption energy of CO on H-MoO_{3-x}@Ru is −2.72 eV, which is significantly stronger than the adsorption energy of −0.68 eV on the surface of MoO_3@Ru. After the adsorption of CO, the band gap of MoO_3@Ru changed from the original 0.54 to 0.81 eV [Fig. 6(c)]. The analysis of the differential charge distribution revealed that CO lost 0.01 electrons. In contrast, the adsorption of CO led to a reduction in the E_g of H-MoO_{3-x}@Ru from 0.38 to 0.26 eV [Fig. 6(f)]. Simultaneously, CO was found to lose 0.07 electrons during this process. It can be inferred that the incorporation of the Ru component into defective MoO_{3-x} significantly enhances the detection capability for CO gas.

3.4 CO experimental sensitivity of H-MoO_{3-x}@Ru

2D defective MoO_{3-x} was exfoliated via supercritical CO_2 (SC CO_2) technology.(31) To investigate the morphology and composition of the sample, TEM was employed.(32) The TEM

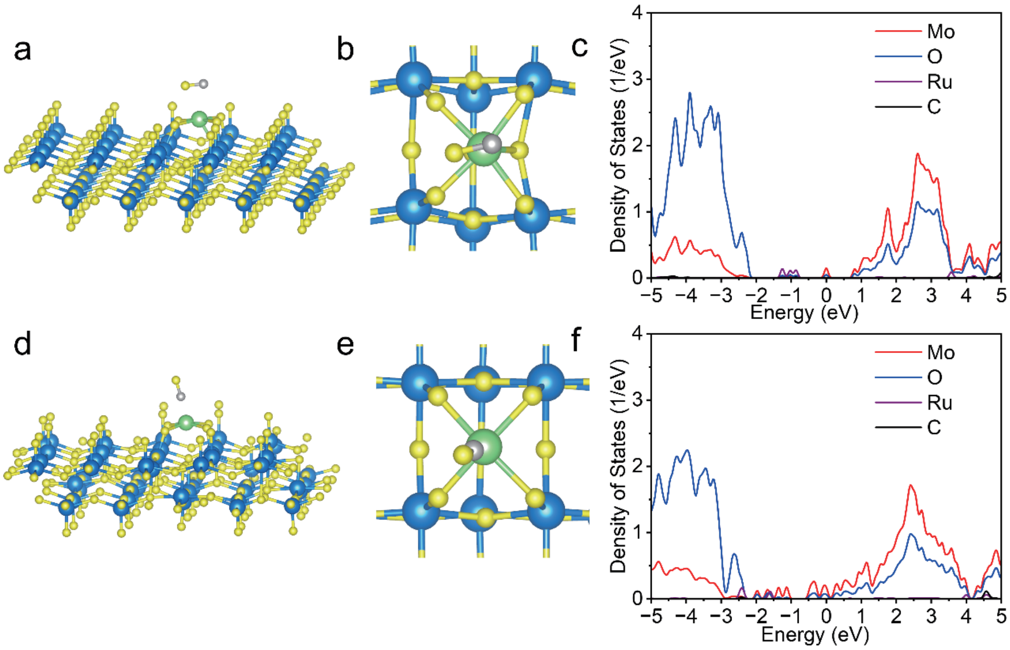

Fig. 6. (Color online) (a, b) CO adsorption model of MoO_3@Ru. (c) DOS diagram of the corresponding model of MoO_3@Ru. (d, e) CO adsorption model of H-MoO_{3-x}@Ru. (f) DOS diagram of the corresponding model of H-MoO_{3-x}@Ru. The blue atom is Mo, the yellow atom is O, and the gray atom is C.

image [Fig. 7(a)] shows uniformly dispersed nanoparticles on the H-MoO_{3-x} carrier, likely corresponding to reduced Ru species. High-resolution TEM (HRTEM) analysis [Fig. 7(b)] reveals distinct structural features in different nanoparticle regions. Figure. 7(c) shows magnified HRTEM regions and their corresponding fast Fourier transform (FFT) patterns. The FFT analysis confirms the coexistence of metallic Ru^0 [hexagonal lattice, d-spacing: 0.207 nm, (101) plane].(33) Energy-dispersive X-ray spectroscopy (EDS) mapping of samples [Fig. 7(d)] confirms the homogeneous distribution of Ru on the H-MoO_{3-x}. Quantitative analysis yields a Ru mass ratio of 2.62 wt%, aligning with the target loading of 2 wt%. To verify accuracy, inductively coupled plasma mass spectrometry (ICP-MS) was performed, revealing a Ru content of 2.45 wt% in the composite. The ICP-MS results are consistent with EDS data, confirming successful Ru loading.

To demonstrate the low-power-consumption advantage of the material, gas sensitivity tests were conducted on the synthesized material under controlled conditions of 25 °C room temperature and 23% humidity. The H-MoO_{3-x}@Ru sensor exhibited a sensitive response to CO, which was investigated by exposing the sensor to CO gas at various concentrations. Figure 7(e) shows the resistance–time response curves of the sensor when exposed to CO concentrations ranging from 60 to 180 ppm. The sensor exhibits a response time of 10 s and a recovery time of 20 s. Figure 7(f) shows the linear correlation between the sensor's sensitivity to CO and the gas concentration. As the CO concentration increases from 60 to 180 ppm, a strong linear correlation ($R^2 = 0.997$) exists between the sensor response (Y) and the CO concentration (X), described by the equation $Y = 0.34X - 3.92$. Additionally, the detection limit of the sensor is estimated to be as low as 12 ppm, demonstrating its high sensitivity to CO.

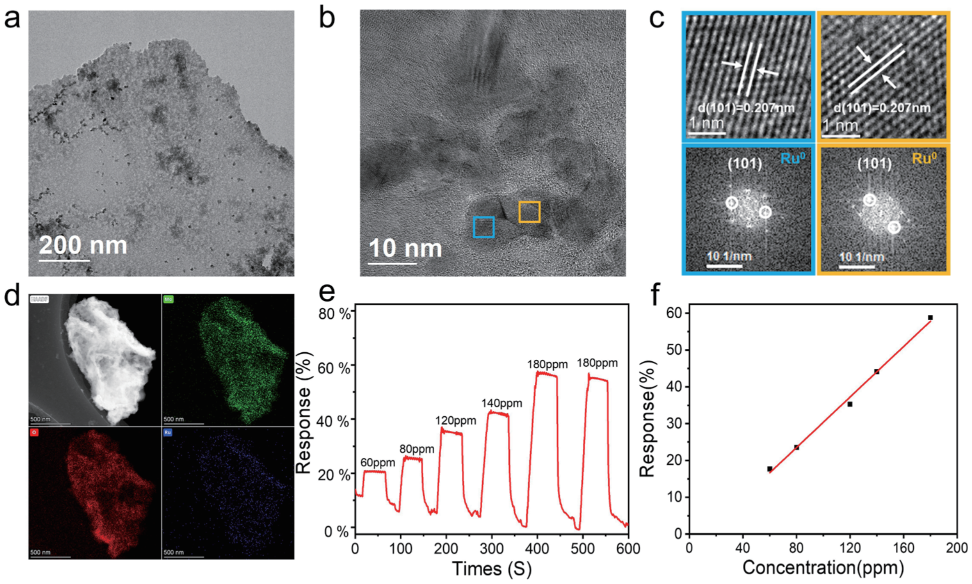

Fig. 7. (Color online) (a) Low-magnification TEM images of H-MoO_{3-x}@Ru. (b) HRTEM images of H-MoO_{3-x}@Ru. (c) Corresponding magnified areas and FFT plots of H-MoO_{3-x}@Ru. (d) EDS mapping of H-MoO_{3-x}@Ru. (e) Dynamic response to CO concentrations (60–180 ppm). The response (%) is defined as (Ra − Rg)/Rg, where Rg and Ra are the resistance values of the gas sensor when exposed to the target gas and air, respectively (f) Calibration curve of sensor response versus CO concentration.

4. Conclusions

The adsorption performance and gas sensitivity mechanism of different types of molybdenum oxide and Ru-doped species for dissolved gas CO, C_2H_2, and H_2 in oil-immersed transformers were studied using first-principles calculations integrated with experimental investigations. The sensitivities of MoO_3, MoO_{3-x}, MoO_3@Ru, and H-MoO_{3-x}@Ru to the dissolved gas CO, C_2H_2 and H_2 in transformer oil were investigated by analyzing their adsorption energy, charge density, and band structure. Oxygen vacancies in molybdenum oxide enhance its adsorption capacity for CO molecules, resulting in significant changes in electrical conductivity. The H-MoO_{3-x} system has a high carrier density, and the adsorption of C_2H_2 has little effect on the electronic structure of the matrix, which is not suitable for practical applications. The end oxygen position and the defect oxygen position are the most stable fixation sites for MoO_3@Ru and MoO_{3-x}@Ru. The H-MoO_{3-x}@Ru system has good adsorption performance for CO and can be used as a sensor for CO detection. The findings presented in this work indicate that molybdenum oxide systems doped with Ru are promising candidates for dissolved gas detection in petroleum.

Acknowledgments

The authors are grateful for the support from the Science and Technology Project of China Southern Power Grid (GDKIXMM20210023).

Conflicts of Interest

The authors declare no conflicts of interest.

References

1 S. Rezaie, Z. G. Bafghi, N. Manavizadeh, and S. B. Kordmahale: IEEE Sens. J. **22** (2022) 82. https://doi.org/10.1109/jsen.2021.3126654
2 T. Jiang, C. Liu, C. Wang, H. Wu, M. Bi, X. Chen, and J. He: Sens. Actuators, A **377** (2024) 115742. https://doi.org/10.1016/j.sna.2024.115742
3 J. Gao, F. Chen, C. Xue, C. Hu, and L. Lin: Flatchem **47** (2024) 100706. https://doi.org/10.1016/j.flatc.2024.100706
4 J. Jiang, D. Yang, W. Zeng, Z. Wang, and Q. Zhou: Front. Chem. **12** (2024) 1507905. https://doi.org/10.3389/fchem.2024.1507905
5 D. Zeng and D. Zhang: Chem. Phys. Lett. **832** (2023) 140886. https://doi.org/10.1016/j.cplett.2023.140886
6 D. Chen, Y. Li, S. Xiao, C. Yang, J. Zhou, and B. Xiao: Appl. Surf. Sci. **579** (2022) 152141. https://doi.org/10.1016/j.apsusc.2021.152141
7 R. Peng, W. Zeng, and Q. Zhou: Appl. Surf. Sci. **615** (2023) 156445. https://doi.org/10.1016/j.apsusc.2023.156445
8 J. Chen, Z. Wu, M. Xu, Y. Liu, L. Duan, P. Xu, and L. Wu: Chem. Phys. Lett. **863** (2025) 141898. https://doi.org/10.1016/j.cplett.2025.141898
9 S. P. Lee: Sensors **17** (2017) 683. https://doi.org/10.3390/s17040683
10 H. Zhang, W.-G. Chen, Y.-Q. Li, and Z.-H. Song: Front. Chem. **6** (2018) 508. https://doi.org/10.3389/fchem.2018.00508
11 M. S. Ali, A. H. A. Bakar, A. Omar, A. S. A. Jaafar, and S. H. Mohamed: Electr. Power Syst. Res. **216** (2023) 109064. https://doi.org/10.1016/j.epsr.2022.109064
12 J. Dai, B. Luo, X. Shen, W. Han, R. Cui, J. Wu, H. Zhang, W. Xiao, Z. Zhong, L. Dong, and H. Wu: Front. Phys. **13** (2025) 1547563. https://doi.org/10.3389/fphy.2025.1547563
13 A.-M. Aciu, S. Enache, and M.-C. Nitu: Energies **17** (2024) 2331. https://doi.org/10.3390/en17102331
14 J. Huang and Q. Wan: Sensors **9** (2009) 9903. https://doi.org/10.3390/s91209903
15 C. H. Kuru, C. M. Choi, A. Kargar, D. Y. Choi, Y. J. Kim, C. H. Liu, S. Yavuz, and S. Jin: Adv. Sci. **2** (2015) 1500004. https://doi.org/10.1002/advs.201500004
16 N. Yi, Z. Cheng, H. Li, L. Yang, J. Zhu, X. Zheng, Y. Chen, Z. Liu, H. Zhu, and H. Cheng: Mater. Today Phys. **15** (2020) 100265. https://doi.org/10.1016/j.mtphys.2020.100265
17 R. Kumar, W. Zheng, X. H. Liu, J. Zhang, and M. Kumar: Adv. Mater. Technol.-US **5** (2020) 1901062. https://doi.org/10.1002/admt.201901062
18 B. Mondal, M. S. Meetei, J. Das, C. Roy Chaudhuri, and H. Saha: Eng. Sci. Technol. **18** (2015) 229. https://doi.org/10.1016/j.jestch.2014.12.010
19 D. Zappa, V. Galstyan, N. Kaur, H. Arachchige, O. Sisman, and E. Comini: Anal. Chim. Acta **1039** (2018) 1. https://doi.org/10.1016/j.aca.2018.09.020
20 Z. Wei, L. Xu, S. Peng, and Q. Zhou: Front. Chem. **8** (2020) 188. https://doi.org/10.3389/fchem.2020.00188
21 Y. Gui, W. Li, X. He, Z. Ding, C. Tang, and L. Xu: Appl. Surf. Sci. **507** (2020) 145163. https://doi.org/10.1016/j.apsusc.2019.145163
22 L. Liu, P. Zhou, X. Su, Y. Liu, Y. Sun, H. Yang, H. Fu, X. Qu, S. Liu, and S. Zheng: Sens. Actuators, B **351** (2022) 130983. https://doi.org/10.1016/j.snb.2021.130983
23 H. Liu, F. Wang, K. Hu, T. Li, and Y. Yan: Appl. Surf. Sci. **590** (2022) 153122. https://doi.org/10.1016/j.apsusc.2022.153122
24 X. Wang, Y. Gui, Z. Ding, H. Xu, H. Zeng, and X. Chen: Surf. Interfaces **31** (2022) 101994. https://doi.org/10.1016/j.surfin.2022.101994
25 A. Hermawan, N. L. W. Septiani, A. Taufik, B. Yuliarto, Suyatman, and S. Yin: Nanomicro Lett. **13** (2021) 207. https://doi.org/10.1007/s40820-021-00724-1
26 P. Bisht, A. Kumar, I. T. Jensen, M. Ahmad, B. D. Belle, and B. R. Mehta: Sens. Actuators, B **341** (2021) 129953. https://doi.org/10.1016/j.snb.2021.129953
27 X. Li, D. S. Jiang, Y. Z. Fan, N. Zhang, C. X. Liu, S. Adimi, J. R. Zhou, S. P. Wen, and S. P. Ruan: Inorg. Chem. Front. **7** (2020) 1704. https://doi.org/10.1039/d0qi00019a

28 W. Li, K. Xing, P. Liu, C. Chuang, Y.-R. Lu, T.-S. Chan, T. Tesfamichael, N. Motta, and D.-C. Qi: Adv. Mater. Technol.-US **7** (2022) 2100579. https://doi.org/10.1002/admt.202100579
29 J. X. Wang, Q. Zhou, Z. J. Wei, L. N. Xu, and W. Zeng: Ceram. Int. **46** (2020) 29222. https://doi.org/10.1016/j.ceramint.2020.08.096
30 S. Q. Wang, J. Xie, J. D. Hu, H. Y. Qin, and Y. L. Cao: Appl. Surf. Sci. **512** (2020) 145722. https://doi.org/10.1016/j.apsusc.2020.145722
31 W. Liu and Q. Xu: Chem. Eur. J. **24** (2018) 13693. https://doi.org/10.1002/chem.201801055
32 W. Liu, Q. Xu, W. Cui, C. Zhu, and Y. Qi: Angew. Chem. Int. Ed. **56** (2017) 1600. https://doi.org/10.1002/anie.201610708
33 H. Fan, X. Wan, S. Sun, X. Zhou, X. Bu, J. Ye, R. Bai, H. Lou, Y. Chen, J. Gao, J. Zhang, W. Gao, and D. Wen: Adv. Energy Mater. **15** (2025) 2405681. https://doi.org/10.1002/aenm.202405681